



Indian Institute of Technology, Bombay

# Tomographic Reconstruction from Electron Cryo-Microscopic images of Heterogeneous Particles

Ritwick Chaudhry

Undergraduate thesis  
under the guidance of

**Prof. Ajit Rajwade**

January 2018

# Contents

<b>1</b>	<b>Introduction</b>	<b>1</b>
1.1	Background . . . . .	1
1.1.1	Computed Tomography . . . . .	1
1.1.2	The Radon Transform . . . . .	1
1.1.3	Fourier Slice Theorem . . . . .	2
1.1.4	Filtered Backprojection . . . . .	3
1.1.5	The Reconstruction . . . . .	4
1.2	Tomography under unknown angles . . . . .	5
1.2.1	Moment based approach . . . . .	5
1.2.2	Machine Learning Based Approaches . . . . .	6
1.3	Cryo-EM . . . . .	6
<b>2</b>	<b>Proposed Solution and Results</b>	<b>8</b>
2.1	Denoising the projections . . . . .	8
2.2	Approaches Tried . . . . .	9
2.2.1	Using Compressed Sensing . . . . .	9
2.2.2	Switching to L1 based loss for modelling difference in particles . . . . .	9
2.2.3	Explicit Modelling of Particle Heterogeneity . . . . .	10
2.3	Our Solution . . . . .	10
2.3.1	The Idea . . . . .	10
2.3.2	Minimizing the Loss . . . . .	10
2.4	Results . . . . .	11
<b>3</b>	<b>Future Work</b>	<b>15</b>

# Chapter 1

## Introduction

### 1.1 Background

#### 1.1.1 Computed Tomography

The goal of X-ray computed tomography is to obtain a 3D representation of the internal structure of an object by X-raying the object from many different directions. The X-ray in one direction produces an image whose intensity at a point is proportional to the X-ray energy impinging on that point after it has passed through the subject. The 3D structure is then reconstructed from a given set of such images and the angles at which these images were taken.

This can also be done by generating slices through the body and the 3D representation then can be obtained by stacking the slices. This involves parallel beam X-rays which are incident on a 'slice' of the body part, which produce 1D projections instead of 2D projection images. But such an approach requires high precision CT machines to generate projections of slices.

#### 1.1.2 The Radon Transform

A parallel-ray beam may be modeled by a set of parallel lines inclined at a fixed angle. An arbitrary point in the projection signal is given by the ray-sum along the line from that set of parallel lines passing through that arbitrary point (as shown in figure 1.1).

The ray-sum can be written as a line integral, given by

$$g(\rho_j, \theta_k) = \int_{-\infty}^{\infty} \int_{-\infty}^{\infty} f(x, y) \delta(x \cos \theta_k + y \sin \theta_k - \rho_j) dx dy \quad (1.1)$$

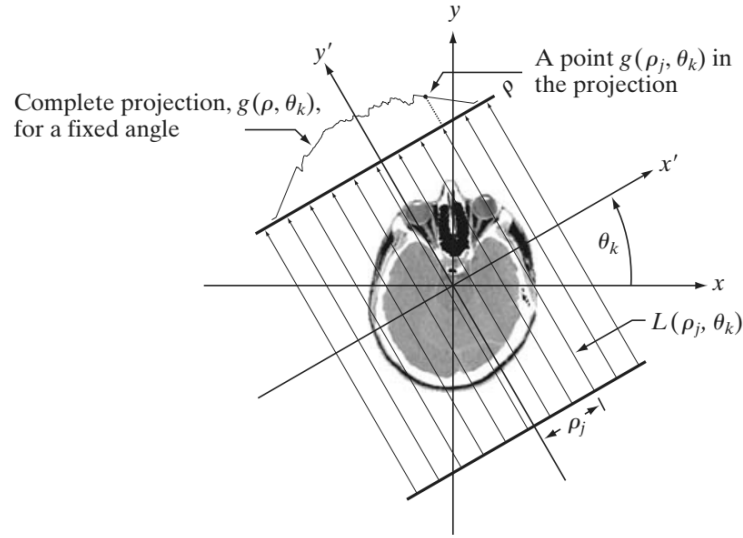


FIGURE 1.1: Parallel Beam X-Ray

Source: Rafael C. Gonzalez , Richard E. Woods, Digital Image Processing (3rd Edition), Prentice-Hall

where  $f(x, y)$  represents the image intensities,  $\theta_k$  is the angle at which the projections are taken and  $\rho_j$  is the distance from the origin.

The Radon Transform is defined as the projection (line integral) of the image along an arbitrary line in the  $xy$ -plane, given by the equation 1.1. The Radon transform of an image  $f(x, y)$  is represented as  $\mathcal{R}\{f(x, y)\}$  in place of  $g(\rho_j, \theta_k)$ .

### 1.1.3 Fourier Slice Theorem

The Fourier Slice Theorem gives a relationship between the 1D fourier transform of a projection of a 2D signal and the 2D transform of the signal itself. The 1D Fourier Transform of a projection at an angle  $\theta$  and distance  $\rho$  from the origin is given by

$$G(\omega, \theta) = \int_{-\infty}^{\infty} g(\rho, \theta) e^{-j2\pi\omega\rho} d\rho \quad (1.2)$$

Substituting for  $g(\rho, \theta)$  from 1.1 in 1.2, we get

$$G(\omega, \theta) = \int_{-\infty}^{\infty} \int_{-\infty}^{\infty} \int_{-\infty}^{\infty} f(x, y) \delta(x \cos \theta + y \sin \theta - \rho) dx dy e^{-j2\pi\omega\rho} d\rho \quad (1.3)$$

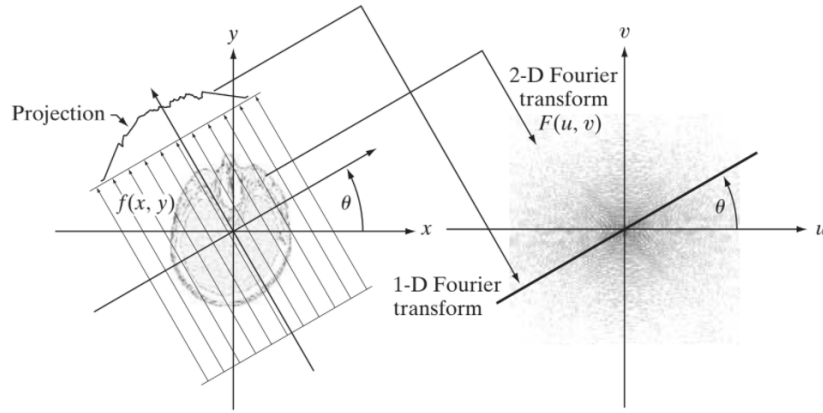


FIGURE 1.2: Fourier Slice Theorem

Source: Rafael C. Gonzalez , Richard E. Woods, Digital Image Processing (3rd Edition),  
Prentice-Hall

$$G(\omega, \theta) = \int_{-\infty}^{\infty} \int_{-\infty}^{\infty} f(x, y) \left[ \int_{-\infty}^{\infty} \delta(x \cos \theta + y \sin \theta - \rho) e^{-j2\pi \omega \rho} d\rho \right] dx dy \quad (1.4)$$

$$G(\omega, \theta) = \int_{-\infty}^{\infty} \int_{-\infty}^{\infty} f(x, y) e^{-j2\pi \omega (x \cos \theta + y \sin \theta)} dx dy \quad (1.5)$$

$$G(\omega, \theta) = [F(u, v)]_{u=\omega \cos \theta, v=\omega \sin \theta} \quad (1.6)$$

where  $F$  denotes the 2D Fourier Transform of  $f$ . Therefore the Fourier Transform of a projection is a slice of the 2D Fourier transform of the region from which the projection was obtained (elucidated in Figure 1.2).

#### 1.1.4 Filtered Backprojection

From the Fourier Slice Theorem, since the 2D fourier transform can be written using the 1D fourier transform of the projections, an inverse fourier transform can be used to reconstruct the original image.

Using the definition of an inverse fourier transform

$$f(x, y) = \int_{-\infty}^{\infty} \int_{-\infty}^{\infty} F(u, v) e^{j2\pi(ux+vy)} du dv \quad (1.7)$$

$$f(x, y) = \int_0^{2\pi} \int_0^\infty F(\omega \cos \theta, \omega \sin \theta) e^{j2\pi\omega(x \cos \theta + y \sin \theta)} \omega \, d\omega \, d\theta \quad (1.8)$$

$$f(x, y) = \int_0^{2\pi} \int_0^\infty F(\omega \cos \theta, \omega \sin \theta) e^{j2\pi\omega(x \cos \theta + y \sin \theta)} \omega \, d\omega \, d\theta \quad (1.9)$$

Substituting for  $G(\omega, \theta)$  from [1.6](#)

$$f(x, y) = \int_0^{2\pi} \int_0^\infty G(\omega, \theta) e^{j2\pi\omega(x \cos \theta + y \sin \theta)} \omega \, d\omega \, d\theta \quad (1.10)$$

$$f(x, y) = \int_0^{2\pi} \int_0^\infty G(\omega, \theta) e^{j2\pi\omega(x \cos \theta + y \sin \theta)} \omega \, d\omega \, d\theta \quad (1.11)$$

Since projections are just flipped if taken from a direction  $180 - \theta$  instead of  $\theta$ ,  $G(\omega, 180 - \theta) = -G(\omega, \theta)$ . Therefore,

$$f(x, y) = \int_0^\pi \int_0^\infty |\omega| G(\omega, \theta) e^{j2\pi\omega(x \cos \theta + y \sin \theta)} \omega \, d\omega \, d\theta \quad (1.12)$$

$$f(x, y) = \int_0^\pi \int_0^\infty |\omega| G(\omega, \theta) e^{j2\pi\omega(x \cos \theta + y \sin \theta)} \, d\omega \, d\theta \quad (1.13)$$

$$f(x, y) = \int_0^\pi \left[ \int_0^\infty |\omega| G(\omega, \theta) e^{j2\pi\omega\rho} \, d\omega \right]_{\rho=x \cos \theta + y \sin \theta} d\theta \quad (1.14)$$

### 1.1.5 The Reconstruction

The Filtered Backprojection Algorithm thus provides a way to reconstruct the image by integrating the inverse 1D Fourier Transforms of the 'filtered' fourier transforms of projections in all directions from 0 to  $\pi$ . Here the filtering is referred to multiplying by  $|\omega|$ , which is called a ramp filter. In principle, the image is recovered by integrating from 0 to  $\pi$ , but in practice a sum over a certain number of angles is taken instead of the integral.

## 1.2 Tomography under unknown angles

Given the projection images and the directions at which they were taken, the image can be reconstructed using the Filtered Backprojection Algorithm. Typically, the knowledge of the angles at which the projections were taken is known. However, there are many scenarios where this may not be the case. For example in cases such as insect tomography, or tomography of objects performing unknown rigid motion, which is equivalent to performing a tomographic reconstruction on a fixed object, with the angles of the projections being unknown. Uncertainty in view angles, though to a lower degree, may also occur due to patient motion in medical imaging.

In each of these scenarios, there may be significant or complete uncertainty in the angles from which tomographic projections are computed. Therefore in such cases, Filtered Backprojection is not a valid way to perform the reconstruction. However, there has been research in this field and there are two main methods for solving this problem:

### 1.2.1 Moment based approach

There are  $n + 1$   $n^{th}$  order moments for the image, for every pair of integers  $p$  and  $q$  such that  $p + q = n$ . The moments are given by

$$v_{p,q} = \int_{-\infty}^{\infty} \int_{-\infty}^{\infty} f(x,y) x^p y^q dx dy \quad (1.15)$$

For any angle  $\theta$ , there exists a single  $n^{th}$  order moment of the projection  $g(\rho, \theta)$  which is given by

$$m_{\theta}^{(n)} = \int_{-\infty}^{\infty} g(\rho, \theta) \rho^n d\rho \quad (1.16)$$

The Helgasson Ludwig Consistency Conditions (HLCC) [1] gives a relationship between the geometric moments of the underlying image  $f(x, y)$  and its projections at a angle.

$$m_{\theta}^{(n)} = \sum_{j=0}^n \binom{n}{j} (\cos\theta)^{n-j} (\sin\theta)^j v_{n-j,j} \quad (1.17)$$

These relations can be used to find out the unknown angles by iteratively solving for the unknown angles and the image moments [2]

### 1.2.2 Machine Learning Based Approaches

Many machine learning approaches have also been applied to this task, but there are a number of assumptions which may not hold true at all. For example, it is assumed in [3] that the projections at nearby angles are similar, and that the angles at which projections are taken are distributed uniformly around a circle. They use Spherical Locally Linear Embedding to embed the projections on a 2D circle. Finally angles are obtained using the 2D projections, sorted and arranged in a uniform manner around the circle.

In [4] a nearest neighbour search is done over the projections to find an ordering of the angles, again assuming that the projections at close angles are similar. Then the obtained angles are uniformly distributed radially.

## 1.3 Cryo-EM

Cryo-EM or cryo-electron microscopy is a tomographic technique used to determine the structure of a molecule or cell [5]. The task involves estimating the 3D density of a target molecule from a large set of images of the molecule (called particle images), obtained with a transmission electron microscope.

In cryo-EM, a purified solution of the target molecule is cryogenically frozen into a thin (single molecule thick) film, and then imaged with a transmission electron microscope. A large number of such samples are obtained, each of which provides a micrograph containing hundreds of visible, individual molecules. In a process known as particle picking, individual molecules are detected, resulting in a stack of cropped particle images. Particle picking is often done manually, however there have been recent attempts to partially or fully automate the process

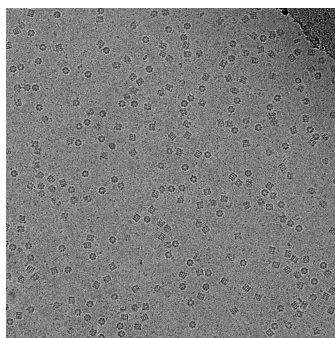


FIGURE 1.3: CryoEM image of GroEL suspended in amorphous ice

Source: [https://en.wikipedia.org/wiki/Cryo-electron\\_microscopy](https://en.wikipedia.org/wiki/Cryo-electron_microscopy)



Most biological specimens are extremely radio sensitive, so they must be imaged with low-dose techniques (usefully, the low temperature of cryo-electron microscopy provides an additional protective factor against radiation damage). Also, the samples of the same virus that are taken on the thin film are not exactly identical and therefore there is an added complexity due to particle heterogeneity. The particles as seen in [1.3](#) are extremely small and often blurred as well.

Consequently, the images are extremely noisy. Each particle image does provide a noisy view of the molecule, but with unknown pose relative to the molecule. On the whole, Cryo-EM brings with it a lot of challenges, including **Noisy Projections**, **Unknown Orientation**, and **Particle Heterogeneity**.

## Chapter 2

# Proposed Solution and Results

### 2.1 Denoising the projections

The first step, involves using a patch-based PCA denoising method to reduce the noise in the projections. This algorithm is adapted from a similar algorithm for 2-D images, as described in [6]. We consider patches of size  $d \times 1$  from a moving window across each projection. For each patch, we find its  $L$  nearest patches (in the L2-norm sense). We perform PCA on this set of  $L$  vectors and project each one along the principal directions to produce eigen-coefficients. To denoise the patch, we manipulate these coefficients using Wiener-like updates of the form

$$\beta_{il} = \alpha_{il} \left( \frac{\sigma_l^2}{\sigma_l^2 + \sigma^2} \right) \quad (2.1)$$

where  $\beta_{il}$  is an estimate of the  $l^{th}$  denoised coefficient for patch  $i$  ( $1 \leq l \leq d$ ),  $\alpha_{il}$  is the corresponding noisy coefficient,  $\sigma^2$  is the noise variance, and  $\sigma_l^2$  is the mean square value of the  $l^{th}$  coefficient estimated as

$$\sigma_l^2 = \max\left(0, \frac{1}{L} (\sum_{i=1}^L \alpha_{il}^2 - \sigma^2)\right) \quad (2.2)$$

We update the patch as well as the  $L$  nearest neighbours. The same patch may be updated twice and therefore each patch is then set as the average of all the denoised values.

## 2.2 Approaches Tried

Note: All the proposed algorithms have been defined for estimation of 2D images of particles and can be easily scaled up to 3D volume estimation

### 2.2.1 Using Compressed Sensing

We formulated an optimization problem embedded in a compressed sensing framework, majorly due to promising results on using compressed sensing. We are also using a PCA based eigenspace, pre-trained on similar images(similarity in structure and not the actual content). The loss function was given by

$$\mathcal{L}(\{\theta_i\}, \beta, \alpha) = \sum_{i=1}^Q \|y_i - \mathcal{R}_{\theta_i}(U\beta)\|_2^2 + \lambda_1 \|\beta\|_1 + \lambda_2 \|V\alpha + \mu - U\beta\|_2^2 + \lambda_3 \|\alpha\|_1 \quad (2.3)$$

where  $\{\theta_i\}_{i=1}^Q$  are the  $Q$  unknown angles at which projections have been taken,  $y_i$  are the actually measured projections along the direction  $\theta_i$ ,  $\mathcal{R}_{\theta_i}$  represents the Radon Transform along the direction  $\theta_i$ ,  $U$  denotes the Inverse DCT operator,  $\beta$  is the vector of DCT coefficients of the image to be reconstructed,  $V$  is the pre-trained eigenspace,  $\mu$  the mean template and  $\alpha$  represents the eigen-coefficients of the image in  $V$

The function was minimized using Alternate minimization over the unknown angles  $\{\theta_i\}_{i=1}^Q$ , the image's DCT coefficients,  $\beta$  and the eigen-coefficients  $\alpha$ .

### 2.2.2 Switching to L1 based loss for modelling difference in particles

Since the above approach didn't explicitly model the particle heterogeneity, we changed the loss to the following function

$$\mathcal{L}(\{\theta_i\}, \beta, \alpha) = \sum_{i=1}^Q \|y_i - \mathcal{R}_{\theta_i}(U\beta)\|_1 + \lambda_1 \|\beta\|_1 + \lambda_2 \|V\alpha + \mu - U\beta\|_1 + \lambda_3 \|\alpha\|_1 \quad (2.4)$$

The idea behind this approach was that the difference of the actual particles from the true particle would be sparse, and therefore even the projections would be sparse. Hence, instead of using L2 norm, L1 norm was used. The same alternating minimization paradigm was used and an L1-L1 solver was applied. The algorithm failed to converge however.

### 2.2.3 Explicit Modelling of Particle Heterogeneity

Next, we moved on to explicitly include the difference in particles, and modelled the loss in the following way

$$\begin{aligned} \mathcal{L}(\{\theta_i\}, \beta, \alpha, \{x_i\}) = & \sum_{i=1}^Q \|y_i - \mathcal{R}_{\theta_i}(U\beta + x_i)\|_2^2 + \lambda_1 \|\beta\|_1 + \lambda_2 \sum_{i=1}^Q \|x_i\|_1 \\ & + \lambda_3 \|V\alpha + \mu - U\beta\|_2^2 + \lambda_4 \|\alpha\|_1 \end{aligned} \quad (2.5)$$

where the loss is now minimized over  $\{x_i\}$  too, which represent the difference in particles.

But using this method, we encountered issues of high computation time and poor performance. This was because estimating  $\{x_i\}$  is extremely hard given a projection at just one angle (that too unknown). We also realized that finding  $\{x_i\}$  is not necessary and that we can do by estimating something much less.

## 2.3 Our Solution

### 2.3.1 The Idea

Finally, we switched from trying to estimate  $\{x_i\}$  to estimating  $z_i \triangleq \mathcal{R}(x_i)$ . We hypothesized that since the difference of the actual and true sample is sparse, so the Radon transform of the difference would be sparse too. Since the dimensions of  $x_i$  are much greater than  $z_i$ , this required less computation time, involved significantly lower degrees of freedom, and hence was a much easier problem to solve. It consequently led to significantly better results.

The final loss function is given by:

$$\begin{aligned} \mathcal{L}(\{\theta_i\}, \beta, \alpha, \{z_i\}) = & \sum_{i=1}^Q \|y_i - z_i - \mathcal{R}_{\theta_i}(U\beta)\|_2^2 + \lambda_1 \|\beta\|_1 + \lambda_2 \sum_{i=1}^Q \|z_i\|_1 \\ & + \lambda_3 \|V\alpha + \mu - U\beta\|_2^2 + \lambda_4 \|\alpha\|_1 \end{aligned} \quad (2.6)$$

### 2.3.2 Minimizing the Loss

We propose an iterative refinement procedure for estimating the unknown orientation, the reconstructed image's DCT coefficients, the Eigen-coefficients and heterogeneity terms which account for the difference in projections due to structural differences in

particles. The algorithm's specification is as follows:

---

```

Initialise  $\alpha = 0$ 
Initialise  $z_i = 0$ , for all  $i$ 
 $\{y_i\} = \text{Denoise\_Projections}(\{y_i\})$ 
 $x = \mu$ 
for  $i=1:Q$ 
     $\theta_i = \text{Best\_Theta}(x, y_i)$ 
end for
while( $x$  converges)
    Solve using an L1-LS Solver:
     $\beta = \text{argmin}(\sum_{i=1}^Q \|y_i - z_i - \mathcal{R}_{\theta_i}(U\beta)\|_2^2 + \lambda_1 \|\beta\|_1 + \lambda_3 \|V\alpha + \mu - U\beta\|_2^2)$ 

    Solve using an L1-LS solver:
     $\alpha = \text{argmin}(\lambda_3 \|V\alpha + \mu - U\beta\|_2^2 + \lambda_4 \|\alpha\|_1)$ 

    Refine particle heterogeneity estimates
    for  $i=1:Q$ 
        Solve for  $z_i = \text{argmin}(\|y_i - \mathcal{R}_{\theta_i}(U\beta) - z_i\|_2^2 + \|z_i\|_1)$ 
        using soft thresholding
         $z_i = \text{softthresh}(y_i - \mathcal{R}_{\theta_i}(U\beta), \lambda_2)$ 
    end for

    Refine Angle Estimates
    for  $i=1:Q$ 
         $\theta_i = \text{Best\_Theta}(x, y_i - z_i)$ 
    end for
end while

```

---

## 2.4 Results

The YALE dataset was used as a toy dataset for testing the algorithm. The eigenspace was trained on 1 face image each of 40 people, and was tested on a different person's face image (A person whose image wasn't present in the templates that were used to train the eigenspace). The size of the images is 192 X 192 pixels, where there is some padding on the sides to make the image square.

To simulate heterogeneous particles, we have add some occluders in the image (black

patches), with the number, size and location of the patches being picked randomly. Also, certain amount of noise is added to the projections, with 10% noise representing addition of gaussian noise with standard deviation of 10% of the average value of the projections.

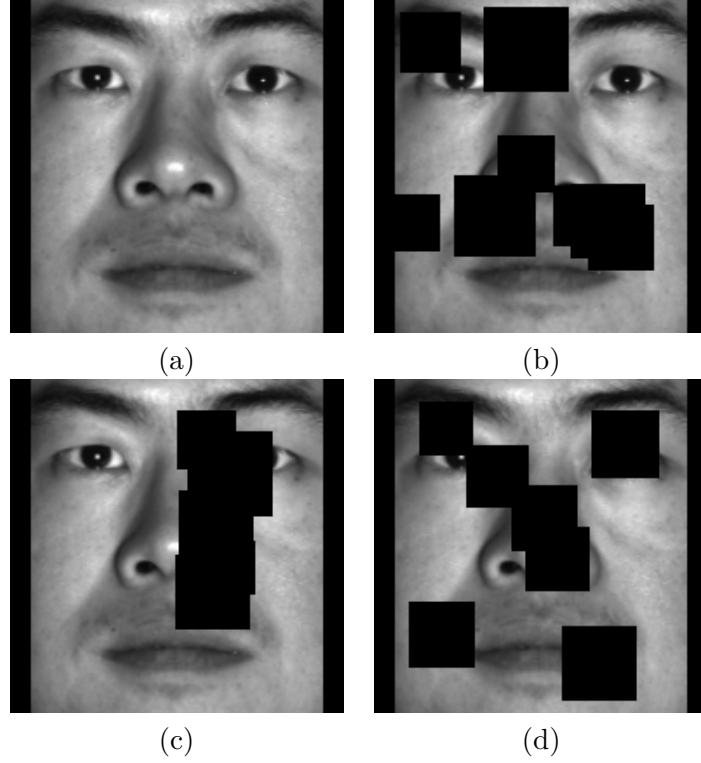
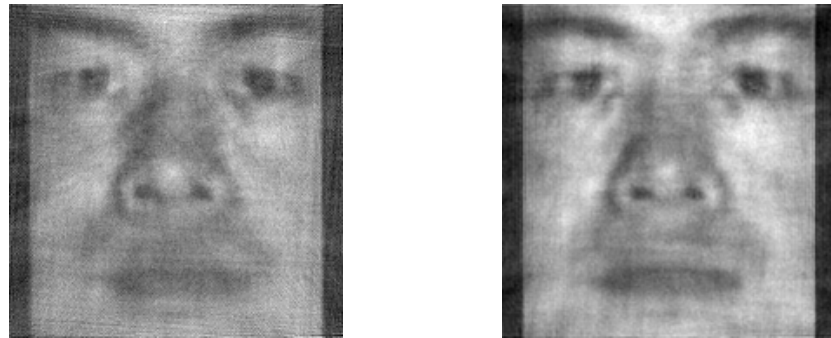


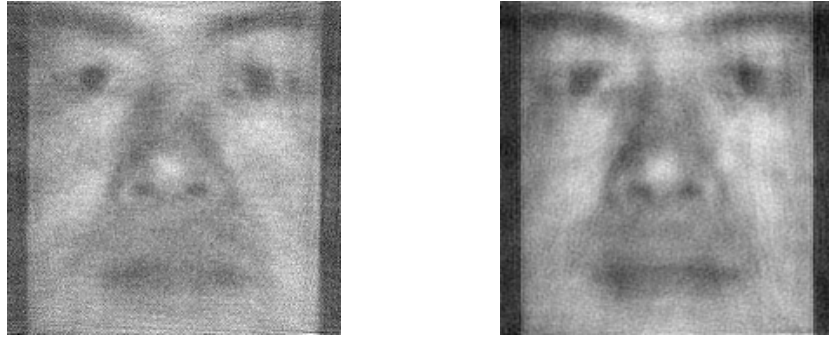
FIGURE 2.1: (a) - The test image — (b),(c),(d) - Occluded samples, each used to generate projection along one direction

Different number and sizes of the occluders are used for the experiments. The difference in performance by modelling the particle heterogeneity explicitly and not including the difference in particles is illustrated as follows:



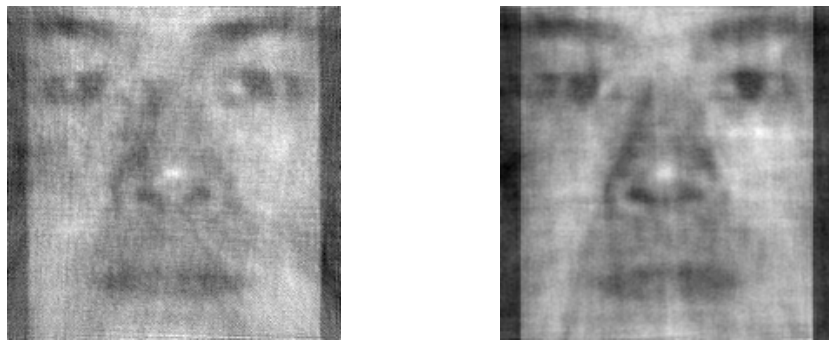
(a) Without modelling the heterogeneity (b) Modelling the heterogeneity

FIGURE 2.2: 200 Angles, 5% Noise, 5% area occluded



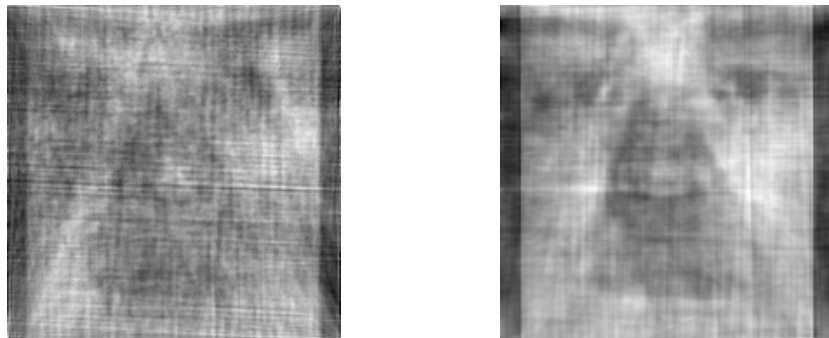
(a) Without modelling the heterogeneity (b) Modelling the heterogeneity

FIGURE 2.3: 200 Angles, 10% Noise, 5% area occluded



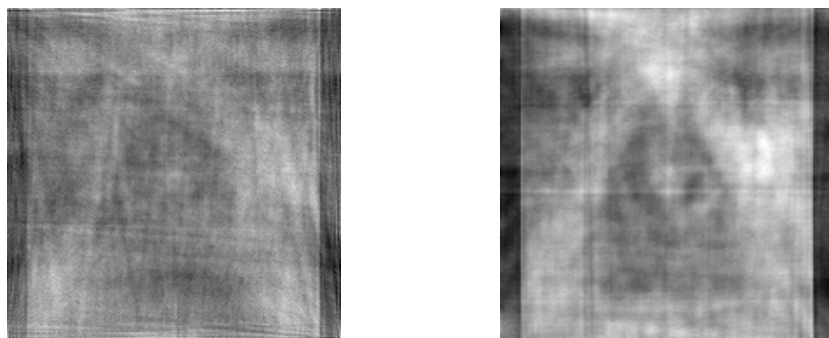
(a) Without modelling the heterogeneity (b) Modelling the heterogeneity

FIGURE 2.4: 200 Angles, 5% Noise, 10% area occluded



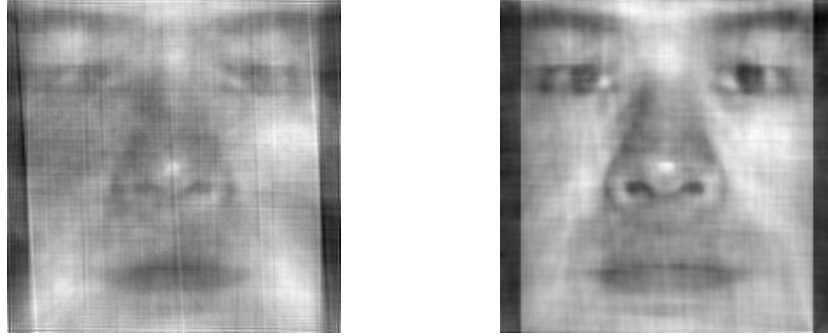
(a) Without modelling the heterogeneity (b) Modelling the heterogeneity

FIGURE 2.5: 200 Angles, 0% Noise, 25% area occluded



(a) Without modelling the heterogeneity (b) Modelling the heterogeneity

FIGURE 2.6: 200 Angles, 5% Noise, 25% area occluded



(a) Without modelling the heterogeneity (b) Modelling the heterogeneity

FIGURE 2.7: 1000 Angles, 0% Noise, 25% area occluded

The results motivate that explicitly modelling of the structural differences in the particles improve the performance. Also, it is evident that the performance of the algorithm modelling the particle heterogeneity shows significant improvement over the algorithm not modelling heterogeneity, as the number of measurements are increased and as the area of the occluders increases. Cryo-EM typically involves a large number of angles and also pathological amounts of noise, and therefore our algorithm can show good performance.



## Chapter 3

# Future Work

The task of performing tomographic reconstruction under unknown angles, high amounts of noise and heterogeneity of particles is a challenging problem, but we have promising results using the proposed algorithm. As of now we have been working in 2D space, taking projections of 2D images. We wish to extend this to 3D Volumes

We are relying on a pre-trained eigenspace and an initialization for the reconstruction using the mean template. We intend to remove the dependence on availability of a set of similar images

The results need to be validated on real cryo-EM datasets, a lot of which are publicly available online [7] provide both micrographs and picked particles (shown in Figure 3.1).

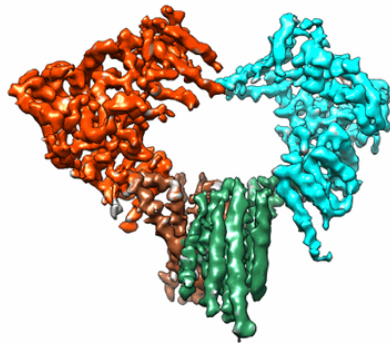


FIGURE 3.1: Cryo-EM structure of Hrd1 and Hrd3 complex

Another feasible dataset to work with was provided in [8] (shown in Figure 3.2).

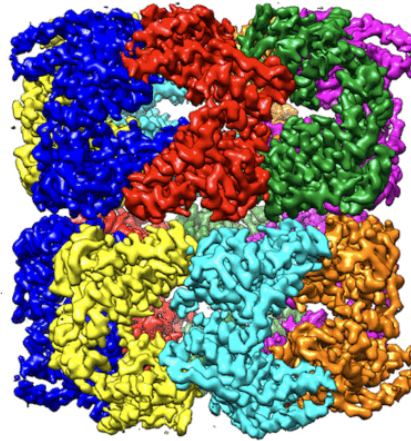


FIGURE 3.2: Structure of GroEL oligomers

# Bibliography

- [1] Frank Natterer. *The mathematics of computerized tomography*. SIAM, 2001.
- [2] Eeshan Malhotra and Ajit Rajwade. Tomographic reconstruction from projections with unknown view angles exploiting moment-based relationships. In *Image Processing (ICIP), 2016 IEEE International Conference on*, pages 1759–1763. IEEE, 2016.
- [3] Yi Fang, Mengtian Sun, SVN Vishwanathan, and Karthik Ramani. sle: Spherical locally linear embedding with applications to tomography. In *Computer Vision and Pattern Recognition (CVPR), 2011 IEEE Conference on*, pages 1129–1136. IEEE, 2011.
- [4] Samit Basu and Yoram Bresler. Feasibility of tomography with unknown view angles. *IEEE Transactions on Image Processing*, 9(6):1107–1122, 2000.
- [5] Joachim Frank. *Three-dimensional electron microscopy of macromolecular assemblies: visualization of biological molecules in their native state*. Oxford University Press, 2006.
- [6] D Darian Muresan and Thomas W Parks. Adaptive principal components and image denoising. In *Image Processing, 2003. ICIP 2003. Proceedings. 2003 International Conference on*, volume 1, pages I–101. IEEE, 2003.
- [7] Stefan Schoebel, Wei Mi, Alexander Stein, Sergey Ovchinnikov, Ryan Pavlovicz, Frank DiMaio, David Baker, Melissa G Chambers, Huayou Su, Dongsheng Li, et al. Cryo-em structure of the protein-conducting erad channel hrd1 in complex with hrd3. *Nature*, 548(7667):352–355, 2017.
- [8] Soung-Hun Roh, Corey F Hryc, Hyun-Hwan Jeong, Xue Fei, Joanita Jakana, George H Lorimer, and Wah Chiu. Subunit conformational variation within individual groel oligomers resolved by cryo-em. *Proceedings of the National Academy of Sciences*, page 201704725, 2017.